CHEMISTRY

Eight-electron Pt/Cu superatom encapsulating three "electron-donating" hydrides

Ayisha He[1], Dongjie Zuo[1], Guangmei Jiang[1], Xiongkai Tang[2], Lin Wang[1], Liubin Feng[2], Zaiwang Zhao[1], Jianyu Wei[3]*, Nanfeng Zheng[2,4]*, Hui Shen[1]*

Hydrides in metal complexes or nanoclusters are typically viewed as electron-withdrawing. Several recent reports have demonstrated the emergence of "electron-donating" hydrides in tailoring the structure, electronic structure, and reactivity of metal nanoclusters. However, the number of such hydrides included in each cluster kernel is limited to one or two. There is even no structure model, neither theoretical nor experimental, for encapsulating a third electron-donating hydride into one cluster entity. Here, we present a structurally precise superatomic nanocluster, PtH_3Cu_{23}(iso-propyl-PhS)$_{18}(PPh_3)_4$ (PtH_3Cu_{23}), which contains three interstitial electron-donating hydrides. The molecular structure of PtH_3Cu_{23} describes the encapsulation of a $PtCu_{12}$ core that contains three interstitial hydrides in a distorted anticuboctahedral architecture, in an outer sphere consisting of copper atoms and thiolate and phosphine ligands. Density functional theory calculations reveal that the three hydrides in PtH_3Cu_{23} contribute their valence electrons to the cluster superatomic electron count of eight. In this regard, the cluster represents a rare Pt-included copper-hydride superatom with eight free electrons.

INTRODUCTION

The pursuit of atomically precise metal nanoclusters relies on the knowledge that not only can their size, composition, structure, and properties be precisely tailored but also substantial atomistic insight into structure-property relationships can be gained (*1*, *2*). Over the past few decades, various gold and silver nanoclusters have been reported, benefiting from their high stability. The correlations between their molecular structures (geometric, electronic, and surface) and physicochemical properties (stability, catalytic activity, luminescence, etc.) have been extensively studied (*3*, *4*). Many of them, being viewed as superatoms (*5*–*7*), i.e., species whose electronic structure mimics that of atoms, (*5*–*7*) have a "magic" number of "free" electrons (2, 8, 18, 20, 34…) providing them with closed-shell stability like noble gases. Conversely, only a handful of superatomic copper clusters have been structurally determined (*8*–*12*), probably due to stability issues introduced by copper hydride nanoclusters (*13*, *14*). Moreover, the application scope of copper nanoclusters is rather limited, mainly being applied in electrocatalysis and reduction reactions (*15*–*17*). It even remains a great challenge for modern synthetic chemists to stabilize high-nuclearity copper-hydride superatoms using the "wet-chemistry" strategy (*8*, *18*). Therefore, more research on copper-hydride nanoclusters (CHNCs) is needed, especially those with distinct compositions, structures, and properties (*19*).

Incorporating a precise number of heteroatoms into the structure is one of the most efficient strategies for tuning the optical, electronic, and catalytic properties of metal nanoclusters (*20*, *21*). Heteroatoms such as Pd and Pt have frequently been introduced into gold- or silver-based nanoclusters to enhance their stability and catalytic activity (*22*, *23*). Well-known examples include Pt-alloyed $PtAu_{24}(SR)_{18}$, which displays higher electrocatalytic activity in hydrogen production compared to the homometallic counterpart, and Pd-alloyed $[PdAg_{20}\{S_2P(O^nPr)_2\}_{12}]$, which exhibits enhanced stability against degradation (*24*, *25*). However, studies on the alloying chemistry of CHNCs are quite limited. Very recently, Liu and coworkers (*26*) isolated three hydride-containing heteroatom alloyed CHNCs, including two Cu(I) species ($[PtH_2Cu_{14}\{S_2P(O^iPr)_2\}_6(CCPh)_6]$ and $[PtH_2Cu_{11}\{S_2P(O^iPr)_2\}_6(CCPh)_3]$) and one two-electron superatom ($[PtHCu_{11}\{S_2P(O^iPr)_2\}_6(CCPh)_4]$). To the best of our knowledge, no other Pt-alloyed CHNCs have been reported so far, although a few related Pd alloys are known (*27*, *28*).

It is generally assumed that when hydrogen acts as a ligand in a metal complex or metal cluster, it is a hydride (H^-), meaning that it has formally withdrawn one electron from the metal(s) (*16*, *29*–*32*). However, in certain specific cases, when encapsulated within superatoms, the hydrogen behaves as a heterometal, i.e., meaning it is a full constituent of the superatomic core and donates its electron to the cluster instead of withdrawing it. These "hydrides" can be considered as "electron-donating" hydrides, as they behave somewhat similarly to the metal atoms that constitute the cluster core (*33*). So far, only a limited number of superatoms containing hydrides, in which the hydrogen electron contributes to the magic electron count, have been identified (*27*, *33*–*40*). Tsukuda and coworkers synthesized the earliest example, the eight-electron $[PdHAu_{10}(PMe_3)_8Cl_2]^+$ complex (*38*). Subsequently, Liu and coworkers (*26*, *27*, *36*) reported several bimetallic Pd/Pt-Cu or Pd/Pt-Ag clusters with two or eight electrons, which contained one or two encapsulated hydrogens, including $[PdHCu_{11}\{S_2P(O^iPr)_2\}_6(C{\equiv}CPh)_4]$,$[PtH_2Cu_{14}\{S_2P(O^iPr)_2\}_6(CCPh)_6]$, and $[PtHAg_{19}(dtp/dsep)_{12}]$ [where dtp is $S_2P(O^nPr)_2$ and dsep is $Se_2P(O^iPr)_2$]. Yi *et al.* (*35*) recently demonstrated the possibility to encapsulate more than one electron-donating hydride in alloyed silver superatoms in their study of $[M@Ag_{24}(SPhMe_2)_{18}]^{2-}$ (M = RhH, IrH, RuH_2, and OsH_2) clusters. Similarly, Chiu *et al.* (*41*) explored the encapsulation of electron-donating hydrides in $[RhH_x@Ag_{21-x}\{S_2P(O^nPr)_2\}_{12}]$

[1]College of Energy Materials and Chemistry, Inner Mongolia University, Hohhot 010021, China. [2]New Cornerstone Science Laboratory, State Key Laboratory for Physical Chemistry of Solid Surfaces, Collaborative Innovation Center of Chemistry for Energy Materials, and National and Local Joint Engineering Research Center of Preparation Technology of Nanomaterials, College of Chemistry and Chemical Engineering, Xiamen University, Xiamen 361005, China. [3]School of Materials and New Energy, Ningxia University, Yinchuan, Ningxia 750021, China. [4]Innovation Laboratory for Sciences and Technologies of Energy Materials of Fujian Province (IKKEM), Xiamen 361102, China.
*Corresponding author. Email: shen@imu.edu.cn (H.S.); jianyu.wei@nxu.edu.cn (J.W.); nfzheng@xmu.edu.cn (N.Z.)

($x = 0$ to 2) clusters. These findings strongly encourage further exploration of the limitations on the number of electron-donating hydrides that can be accommodated within a metal cluster cage.

We hereby report an unprecedented Pt-centered, eight-electron superatomic copper nanocluster, PtH_3Cu_{23}(iso-propyl-PhS)$_{18}$(PPh_3)$_4$ (abbreviated as PtH_3Cu_{23} hereafter), that encapsulates three electron-donating hydrides. The synthesis of PtH_3Cu_{23} is rather simple, involving a one-step reduction of Pt and Cu salts in the presence of thiolate ligands. The molecular structure of PtH_3Cu_{23} is determined by x-ray single-crystal diffraction (SCXRD), and its composition is confirmed by high-resolution electrospray ionization mass spectrometry (HR-ESI-MS). The overall structure of PtH_3Cu_{23} adopts a quasi-tetrahedral architecture, with the PtH_3 heterostructure confined in the center of an anticuboctahedral Cu_{12} kernel. Such an arrangement exhibits noticeable differences from previously reported mono- or dihydride containing icosahedral M_{12} kernel (*34*–*36*). Density functional theory (DFT) calculations reveal that the three hydrides contribute their valence electrons to the cluster's superatomic electron count, which totals eight, making it a superatom which contains three interstitial electron-donating hydrides.

RESULTS

Synthesis and characterization of PtH_3Cu_{23}

The synthesis of a cluster entity that can encapsulate more than two electron-donating hydrides has proven to be challenging. Previous reports have shown that the metal core used for encapsulating such hydrides is typically based on an M_{12} icosahedron (M is Au or Ag; fig. S1) (*27*, *28*, *34*–*36*, *38*, *41*). As predicted by Hu *et al.* (*33*), the adsorption energies of the third hydrogen atom on the icosahedral core would be much weaker, which somehow prevents the formation of stable cluster kernel with three (and more) electron-donating hydrides encapsulation. It thus occurs to us that the key to incorporate more electron-donating hydrides into the M_{12} entity is to introduce other architectures that have a larger volume (such as the anticuboctahedron) (*1*). To create an anticuboctahedral core with sufficient space for incorporating more electron-donating hydrides, we turned our attention to CHNCs. The core structure of CHNCs often differs from that of Au and Ag counterparts (*16*). On the other hand, Pt is introduced in the synthesis to induce the formation of electron-donating hydrides in CHNCs. It is important to note that the proton nuclear magnetic resonance (^{1}H NMR) of Pt-H units, which often display an unresolved resonance flanked with platinum satellites, allows for the detection of PtH-alloyed CHNCs in the synthesis (vide infra) (*36*).

To obtain Pt-alloyed CHNCs including more electron-donating hydrides, we have carefully sieved the precursors. Here, H_2PtCl_6 was used as the Pt source, and we tested 26 representative copper salts for the synthesis. The raw products synthesized through the co-reduction of H_2PtCl_6 and copper salts in the presence of ligands were characterized using ^{1}H NMR. As shown in figs. S2 and S3 and table S1, certain amino acid copper salts [such as Cu(L-valine)$_2$ and Cu(L-isoleucine)$_2$] can afford the PtH_3Cu_{23} cluster, characterized by a triple satellite peak at −4.05 parts per million (ppm). Moreover, not all copper salts can yield the cluster, as evidenced by the absence of the characteristic peaks in the products synthesized from Cu(L-alanine)$_2$ and Cu(CH_3COO)$_2$. Notably, a more complex sextet is observed in the product prepared from Cu($MeCN$)$_4BF_4$ and Cu(CF_3COO)$_2$, which strongly indicating the presence of more complex coordination structures between hydrides and metal atoms. These discoveries not only demonstrate the coordination diversity of electron-donating hydrides in metal nanoclusters but also cultivate a fertile soil for studying the coordination chemistry of electron-donating hydrides in metal nanostructures.

The synthesis of PtH_3Cu_{23} typically involves the Cu(PPh_3)$_2BH_4$-mediated direct reduction of H_2PtCl_6 and Cu(L-valine)$_2$ in the presence of appropriate amounts of thiolate ligands (see Materials and Methods and fig. S4 for details). In contrast to previously reported strategies for obtaining Pd-containing CHNCs where syntheses are carried out under an inert atmosphere, PtH_3Cu_{23} is prepared in air (*27*, *28*). In a typical synthesis, H_2PtCl_6 is added to a suspension of Cu(L-valine)$_2$ in a mixed solvent of methanol and dichloromethane. After adding 4-isopropylphenthiol, a turbid solution is obtained, which turns from gray green to reddish brown upon the addition of Cu(PPh_3)$_2BH_4$. After aging the reaction for 3 hours, a red solution along with some insoluble by-products is obtained. The final product is crystallized from the diffusion of ether into the reddish raw solution over a period of 2 weeks (fig. S5). After a series of purification steps, the resulting clean crystals were used for all subsequent experimental studies.

Copper nanoclusters often include hydrides in their structures (*14*, *42*). To determine the exact number of hydrides in the PtH_3Cu_{23} cluster and confirm its molecular formula, we prepared PtH_3Cu_{23} and PtD_3Cu_{23} and characterized them using HR-ESI-MS. The samples, dissolved in dichloromethane, were analyzed in the positive ion mode. For PtH_3Cu_{23}, the peak with the highest abundance at mass/charge ratio (m/z) = 2778.8210 corresponds to the molecular ion of $[PtH_3Cu_{25}$(iso-propyl-PhS)$_{18}$(PPh_3)$_4]^{2+}$ (calcd m/z = 2778.8; Fig. 1, top). The perfect match between experimental and simulated isotopic patterns suggests the rationality of the molecular identification (Fig. 1, inset). Notably, two Cu^+ ions are added to the parent PtH_3Cu_{23}(iso-propyl-PhS)$_{18}$(PPh_3)$_4$ cluster to form the positive species under the ionization condition. Corresponding to the ESI-MS of PtH_3Cu_{23}, the ESI-MS of PtD_3Cu_{23} shows peaks that are exactly shifted. For example, the prominent peak at m/z 2780.3303 (assigning to $[PtD_3Cu_{25}$(iso-propyl-PhS)$_{18}$(PPh_3)$_4]^{2+}$, calcd m/z = 2780.3) was increased by exactly 1.5 m/z in comparison to $[PtH_3Cu_{25}$(iso-propyl-PhS)$_{18}$(PPh_3)$_4]^{2+}$ (Fig. 1, bottom inset). We have also carefully assigned the molecular formulae of all other prominent peaks in the mass spectra. As shown in fig. S6, all peaks are derived from the parent clusters, although the number of Cu^+ adducts and PPh_3 ligands is tunable.

The presence and coordination chemistry of three hydride atoms in the PtH_3Cu_{23} cluster have been further investigated using ^{1}H NMR spectroscopy at 600 MHz. We have carefully compared ^{1}H NMR spectra of PtD_3Cu_{23} and PtH_3Cu_{23} in CD_2Cl_2, which allows us to isolate signals from the hydride atoms in the PtH_3Cu_{23} sample. As shown in fig. S7, a peak at −4.05 ppm, which shows an unresolved resonance flanked by platinum satellites ($^1J_{1H\text{-}195Pt}$ = 540 Hz), is observed. This suggests that the cluster contains hydride atoms that are tightly coordinated to the Pt center (*36*, *43*). We note that the chemical shift for electron-donating hydrides is highly dependent on cluster structures, as evidenced by the wide range in reported clusters (table S2). Moreover, we have recorded the ^{2}H NMR spectrum of PtD_3Cu_{23} in CH_2Cl_2 (fig. S8). A signal centered at −4.02 ppm was observed in the ^{2}H NMR spectrum of PtD_3Cu_{23}, corresponding to the peak at −4.05 ppm in the ^{1}H NMR spectrum of PtH_3Cu_{23}. To gain deeper insights into the bonding of the three

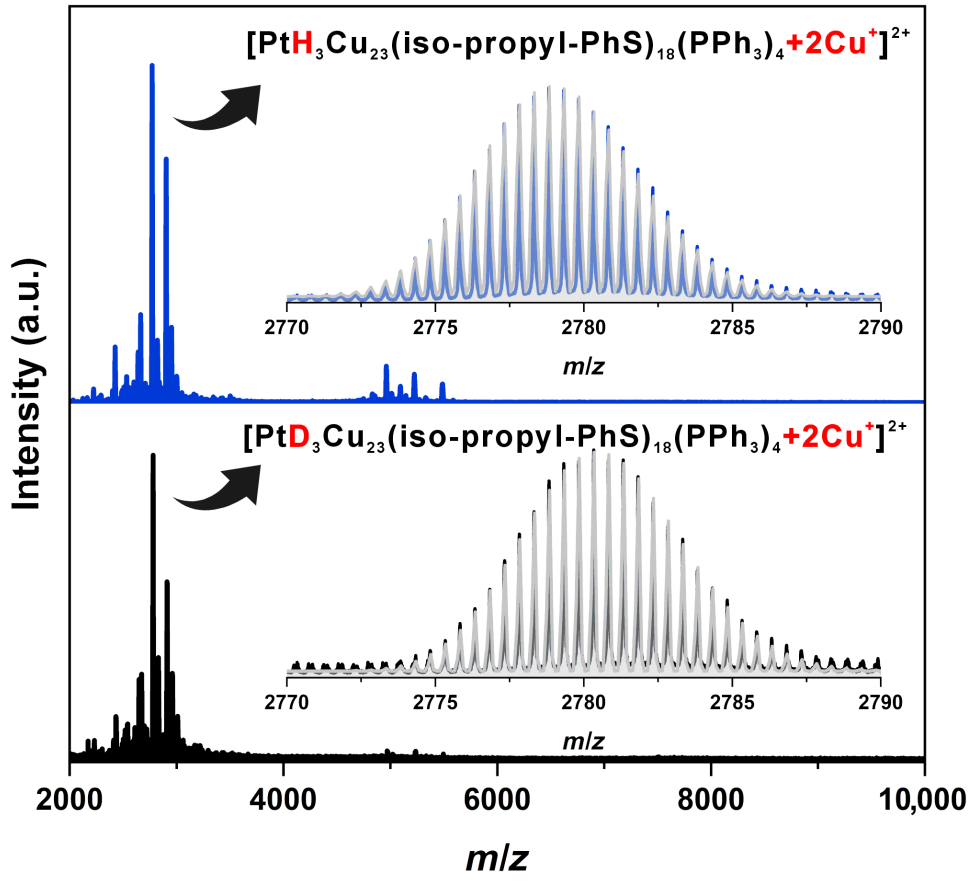

Fig. 1. ESI-MS spectra of PtH_3Cu_{23} and PtD_3Cu_{23} NCs dissolved in dichloromethane solution and measured in the positive mode. Inset: Experimental (black and dark green) and simulated (red) isotopic distributions of $[PtH_3Cu_{25}(iso\text{-}propyl\text{-}PhS)_{18}(PPh_3)_4]^{2+}$ (**top**) and $[PtD_3Cu_{25}(iso\text{-}propyl\text{-}PhS)_{18}(PPh_3)_4]^{2+}$ (**bottom**). a.u., arbitrary units.

hydride atoms with the Pt center, we have used variable-temperature (VT) ^{1}H NMR, VT ^{195}Pt{^{1}H}, and ^{1}H {^{195}Pt} decoupling experiment. As shown in fig. S9 (left), the VT ^{1}H NMR spectrum of PtH_3Cu_{23} keeps almost unchanged, suggesting that no isomerization occurs for the cluster (*36*). The ^{195}Pt{^{1}H} NMR spectrum of the cluster exhibits distinct peak at low temperatures (−7931.89 ppm at −20°C and −7610.03 ppm at −40°C), further confirming the presence of Pt atom in the structure (fig. S9, right). The Pt satellites in the ^{1}H{^{195}Pt} NMR spectrum of PtH_3Cu_{23} vanished when the decoupling range is adjusted to −6500 ppm, providing strong evidence for the coordination of hydrides with the Pt atom in the cluster (fig. S10). The observation of a singlet broad peak in proton-decoupled ^{31}P NMR of PtH_3Cu_{23} suggests the rapid exchange of phosphine ligands on the cluster (fig. S11). Furthermore, VT NMR data indicate that the signal becomes broad at low temperature. At room temperature, the exchange rate is much faster than the NMR timescale, and we observed the process approaching a comparable exchanging rate.

X-ray photoelectron spectroscopy (XPS) studies have been used to evaluate the oxidation states of Pt and Cu. The binding energy of Pt $4f_{7/2}$ is 71.8 eV, suggesting the zero-oxidation state of Pt (fig. S12A) (*44*). The Cu $2p_{3/2}$ peak at 932.7 eV indicates the mixed $Cu^{0/+1}$ states of Cu atoms in PtH_3Cu_{23} (fig. S12B). In particular, two peaks at 916.02 and 919.00 eV with the area ratio of 1: 0.48 were present in the Cu Auger electron spectra (fig. S12C). It shows that for the total 23 Cu atoms, ~8 remain Cu^0 state, while ~15 remain Cu^+ state, suggesting a cluster free electron count of eight. This electron count and charge state are further confirmed by subsequent DFT calculations (vide infra). The characterization of PtH_3Cu_{23} solutions in toluene was performed using ultraviolet-visible (UV-vis) spectroscopy. Within the wavelength range of 300 to 800 nm, a distinct shoulder peak was observed only at 495 nm (fig. S13).

Molecular structure of PtH_3Cu_{23} and its electron-donating hydrides

A single-crystal x-ray diffraction (SCXRD) analysis has been performed on PtH_3Cu_{23} to determine its molecular structure (fig. S14). It reveals that the cluster consists of 1 Pt atom, 3 hydride atoms, 23 Cu atoms, 18 4-isopropylmercaptan ligands, and 4 PPh_3 ligands (Fig. 2), forming a cluster of ~2.1 nm in size (fig. S15). The unit cell comprises eight clusters, which crystallize in the cubic $Pa\bar{3}$ space group (fig. S16 and table S3). These hydrides were located on the basis of the residual density peaks in the Fourier difference map, and their precise positions were subsequently refined using the least squares method. Moreover, the predicted positions of the hydrides by this method align well with the previously characterized NMR data, demonstrating good correspondence (*45*).

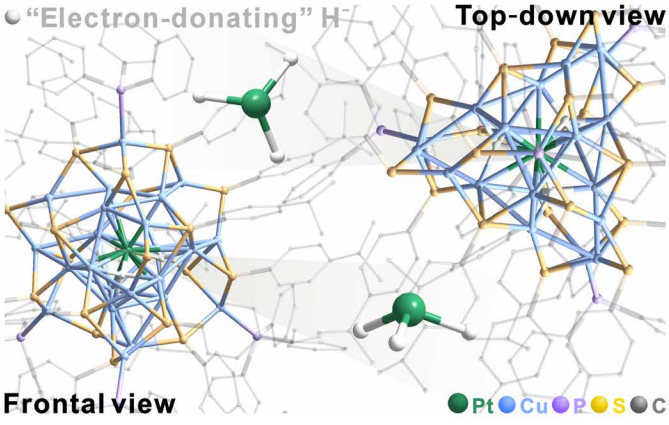

Fig. 2. Total molecular structure of PtH_3Cu_{23}. The bottom left corner represents a frontal view, while the top right corner represents a top-down view. To enhance clarity, all hydrogen atoms, except for the electron-donating hydrides, have been omitted.

The overall structure of PtH_3Cu_{23} is in a quasi-tetrahedral arrangement (Fig. 3A). The structure of the cluster is described as the stabilization of a $[PtH_3Cu_{12}]^{7+}$ core by a Cu_{11}(iso-propyl-PhS)$_{18}$(PPh_3)$_4$ outer shell. The metal kernel consists of a PtH_3-centered Cu_{12} cage (Fig. 3B). The PtH_3Cu_{12} kernel adopts an intermediate geometry between a centered icosahedral and an anticuboctahedral structure (Fig. 3C and fig. S17) (*46*, *47*). This geometry is far from that of the pseudo-icosahedral $M@Ag_{12}$ core found in the previously reported monohydride $[PtHAg_{19}\{S_2P(O^nPr)_2\}_{12}]$ and dihydride $[MH_2@Ag_{24}(SPhMe_2)_{18}]^{2-}$ (M = Ru or Os) clusters, indicating that the icosahedral M_{13} architecture is too small to accommodate more than two hydrides (*35*, *36*). The average Cu—Cu and Pt—Cu bond lengths in the $PtCu_{12}$ core are 2.6252 and 2.7093 Å, respectively, which are comparable to those observed in other nanoclusters (*8*, *44*). It is noteworthy that the Cu_{12} anticuboctahedron is heavily distorted away from the ideal D_{3h} symmetry. Detailed analysis reveals that only a C_3 symmetry axis is present in the $PtCu_{12}$ kernel (Fig. 3C). The amplitude of the distortion of the PtH_3Cu_{12} kernel away from the ideal M_{13} polyhedra was quantitatively analyzed using the continuous symmetry measure (CSM) approach (*48*). By

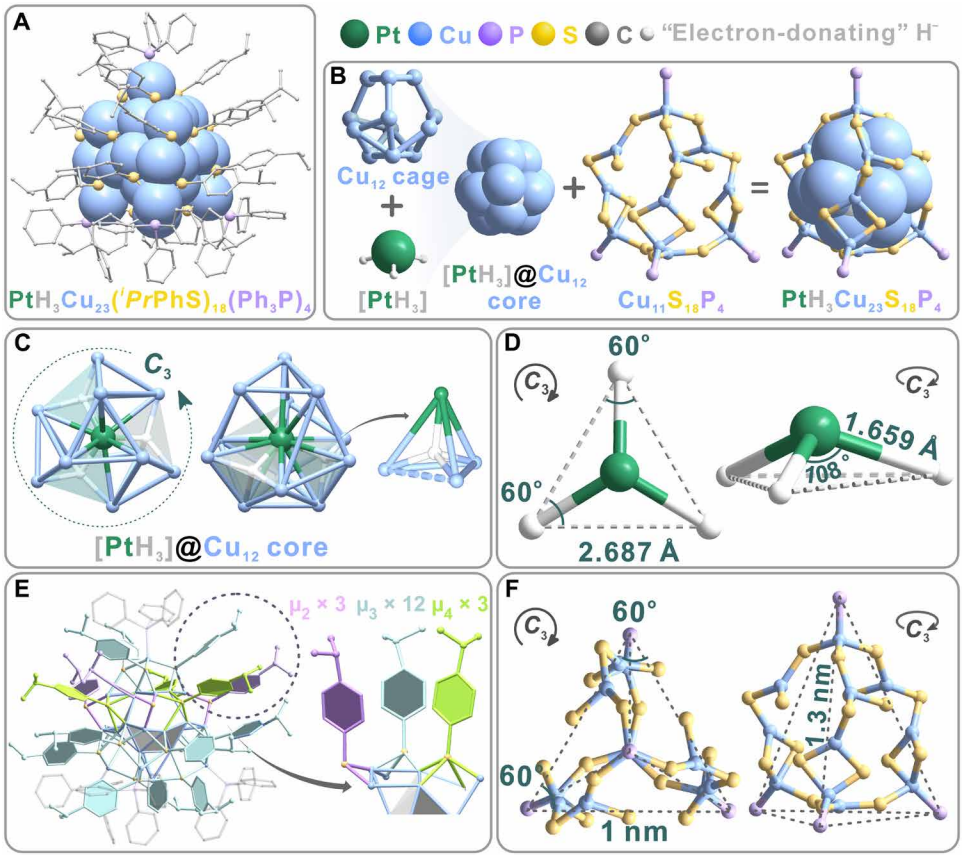

Fig. 3. Structure anatomy of the PtH_3Cu_{23} nanocluster. (**A**) The overall structure of PtH_3Cu_{23} with a quasi-tetrahedral structure. (**B**) The structural anatomy of the PtH_3Cu_{23} cluster, with the benzene rings on the ligands omitted for clarity. (**C**) The structural diagram of the distorted anticuboctahedral metal core in $[PtH_3Cu_{12}]^{7+}$. The core has only a C_3 symmetry axis, with each electron-donating hydride encapsulated within a $PtCu_3$ tetrahedral unit. (**D**) The $[PtH_3]$ unit presents a flattened tetrahedral configuration with a base formed by an equilateral triangle. (**E**) Three coordination modes of the sulfate ligands. (**F**) The distorted tetrahedral protective shell of Cu_{11}(isopropyl-PhS)$_{18}$(PPh_3)$_4$.

comparing the CSM values obtained for the icosahedron (8.1), cuboctahedron (5.2), and anticuboctahedron (4.7), the structure of this $PtCu_{12}$ kernel was found to be closer to an anticuboctahedron (table S4). The large distortion of the Pt-centered Cu_{12} anticuboctahedron is likely due to the presence of the three interstitial hydride atoms within the framework. They are symmetrically distributed around the C_3 symmetry axis (Fig. 3D). Each hydride atom is encapsulated within a $PtCu_3$ tetrahedron, with same values for the Pt-H (1.6594 Å) and Cu-H distances (average, 1.658 Å) (table S5). The three H atoms and the Pt atom form a squashed tetrahedron, with an H-Pt-H angle of 108° (Fig. 3D and table S5). The volume of the $PtCu_3$ unit changes slightly, whether or not it is encapsulated with electron-donating hydrides. As shown in fig. S18, the unit volume with hydride atom encapsulation is 2.27 $Å^3$, while the unit volume without hydride atom encapsulation is 2.28 $Å^3$. Both types of $PtCu_3$ units (pink and blue) are arranged in an axisymmetric manner along the C_3 axis.

The 18 thiolates belonging to the Cu_{11}(iso-propyl-PhS)$_{18}$(PPh_3)$_4$ outer shell can be categorized into three different bridging modes, μ_2, μ_3, and μ_4, respectively (Fig. 3E). The Cu—S bond lengths range from 2.202 to 2.567 Å, giving an average value of 2.224 Å. The entire shell of Cu_{11}(iso-propyl-PhS)$_{18}$(PPh_3)$_4$ also adopts a tetrahedral structure. If the P atoms in the shell are interconnected, then a tetrahedral structure with a base edge length of 1 nm, forming an equilateral triangle, is obtained (Fig. 3F). In addition, clear intermolecular and intramolecular interactions between ^{i}PrPhSH and PPh_3 ligands are observed, such as C—H···π (with centroid distances ranging from 2.77 to 4.01 Å) and π-π interactions (at 3.92 Å). These weak interactions are believed to facilitate the stabilization of the cluster structure (fig. S19).

It is worth noting that the two-electron cuboctahedral superatomic M@Cu_x kernel (M = Cu, PdH, and PtH with x = 11 and 12, respectively) exists (*26*, *46*, *47*), and the eight-electron icosahedral Cu@Cu_{12} kernel (*9*) has also been reported very recently. The centered anticubocahedron reported here is unveiled, suggesting that introducing several interstitial hydrides substantially affects the structure of copper nanoclusters.

Theoretical analysis of PtH_3Cu_{23}

The geometric and electronic structures of PtH_3Cu_{23} were further investigated by DFT calculations at the BP86/STO-TZ2P level (see the "Computational details" section in Materials and Methods). This level of theory has been validated many times in ground-state investigations of noble metals (*49*–*52*). For the sake of computational limits, the iso-propyl-PhS and PPh_3 ligands were simplified by the simple SCH_3 (SMe) and $P(CH_3)_3$ (PMe_3) alternatives, respectively. This kind of simplification has been proven reasonable in many previous investigations (*41*, *53*, *54*). The optimized geometry confirms the SCXRD positions of the interstitial hydrides. The calculated metal-metal distances are comparable to those of the distances measured from the x-ray crystal structure, and the distorted $[PtH_3Cu_{12}]^{7+}$ inner core with the three tetrahedrally coordinated interstitial hydrides is well reproduced (table S4). The optimized structure of the $PtH_3Cu_{23}(SMe)_{18}(PMe_3)_4$ model was found to be of C_3 symmetry, with a computed highest occupied molecular orbital–lowest unoccupied molecular orbital (HOMO-LUMO) gap of 1.21 eV, which is of similar magnitude to that of previously reported copper or silver hydride nanoclusters (*27*, *34*–*38*). Owing to the encapsulation of the three μ_4-H atoms, the Cu_{12} cage of the PtH_3Cu_{12} core is largely distorted (rotated) along the C_3 axis, resulting in the Pt@Cu_{12} kernel having a geometry intermediate between the icosahedral and anticuboctahedral. Detailed analysis of its molecular orbital (MO) diagram (Fig. 4 and fig. S20) indicates that the $PtH_3Cu_{23}(SMe)_{18}(PMe_3)_4$ cluster is an eight-electron superatom within the superatom concept (*5*–*7*). From their shape and composition, the three highest occupied MOs, mainly made of 6s(Pt), 4s(Cu), and 1s(H) atomic orbitals (AOs), can be identified as the superatomic 1P orbitals, with some 3d(Cu) admixture. The five vacant lowest unoccupied MOs are of superatomic 1D characters. The superatomic 1S orbital, mainly made of the 6s(Pt), 4s(Cu), and 1s(H) (~30%) AOs, is fully occupied and situated lower in energy (Fig. 4). This electronic configuration is in agreement with the XPS characterized 1 to 0.48 ratio of Cu^+ to Cu^0 (fig. S12C), indicating that hydrides donating their electrons to the cluster which decrease the charge states of Cu. The computed natural AO (NAO) charges of the 11 periphery Cu_{cap} (~+0.6) indicate a +I oxidation state, which is in agreement with the trigonal-planar coordination of the surface $Cu(SR)_3$ (16-electrons) motif or the linear coordination of the surface $Cu(SR)_2$ (14-electrons) motifs (table S6). The relatively smaller NAO charges of the 12 $Cu_{anticubo}$ (~+0.4) in the Pt@Cu_{12} kernel confirmed their mixed-valence nature (table S7). The hydrides NAO charge (−0.4) is notably lower than that found usually for the regular electron-withdrawing hydrides (−0.45 to −0.71; tables S7 and S8), which is owing to the strong bonding between H and the Pt dopant, whose electronegativity values are larger than that of H (*55*–*60*). In other words, doping such M-H_x unit into a cluster cage may facilitate the electron-sharing behavior of the interstitial hydrides. The subsequent quantum theory of atoms in molecules (QTAIM) analysis further confirmed a charge

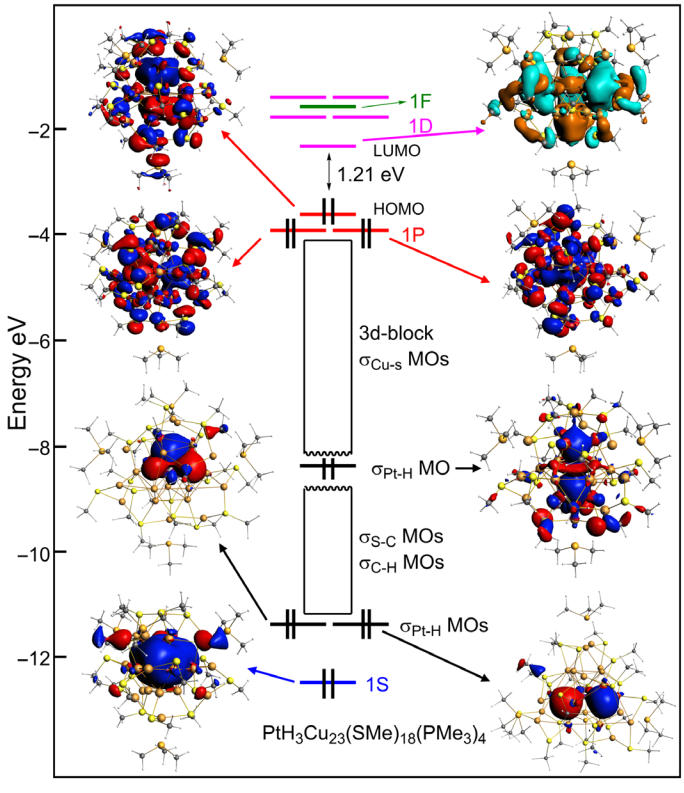

Fig. 4. Kohn-Sham MO diagram of $PtH_3Cu_{23}(SMe)_{18}(PMe_3)_4$. The blue, red, pink, and green sticks represent superatomic 1S, 1P, 1D, and 1F orbitals, respectively.

transfer from the periphery Cu cage to the centered Pt atom (fig. S21). The calculated Bader charge of the hydrides (−0.18) exhibits also a similar trend as found for the NAO analysis (tables S9 and S10). These charge distributions, in combination with the Pt—$Cu_{anticubo}$ (0.072) and $Cu_{anticubo}$—$Cu_{anticubo}$ (0.057) Wiberg bond indices [larger than that of the mainly cuprophilic $Cu_{anticubo}$—Cu_{cap} (0.041) bonds], suggest the description of the PtH_3Cu_{23} made by an eight-electron superatomic $[PtH_3Cu_{12}]^{7+}$ kernel protected by 18 iso-propyl-PhS, 4 PPh_3, and 11 Cu^+ centers, respectively (table S6). In addition, the natural electronic configuration of Pt ($5d^{9.65}6s^{0.76}6p^{0.10}$) indicates a substantial participation of 6s(Pt) AOs into the occupied 1S and 1P superatomic orbitals, whereas the 5d(Pt) population shows a nonnegligible contribution to the unoccupied 1D levels. However, this involvement is not enough to consider PtH_3Cu_{23} as an 18-electron superatom (*35*, *52*, *61*).

The role of the hydrides in the bonding of the superatomic $[PtH_3Cu_{12}]^{7+}$ core can be understood from the simplified qualitative MO diagram sketched in Fig. 5. It describes the interaction between the $[PtCu_{12}]^{7+}$ cage and the encapsulated triangular $[H]_3$ motif. The five-electron $[PtCu_{12}]^{7+}$ fragment is an unstable open-shell superatom, whereas it achieves the eight-electron closed-shell stability after interaction with the encapsulated $[H]_3$ fragment. The $\alpha_1([H]_3)$ combination interacts with the $5d_{z2}$(Pt) AO, and the $e([H]_3)$ combinations interact with the $5d_{xy}$(Pt) and $5d_{x2-y2}$(Pt) AOs, generating three occupied bonding σ_{Pt-H} MOs and three vacant antibonding σ^*_{Pt-H} MOs, thus provoking the complete filling of the superatomic 1P shell in the $[PtH_3Cu_{12}]^{7+}$ core. Therefore, $[PtH_3Cu_{12}]^{7+}$ can be viewed as an eight-electron superatom. The three electron pairs associated with the three σ_{Pt-H} bonds are somewhat delocalized over the whole cluster cage, resulting in a moderate contribution of the 1s(H) AOs to the superatomic orbitals (10 and 4% in total in the 1P and 1D levels, respectively) and a minor

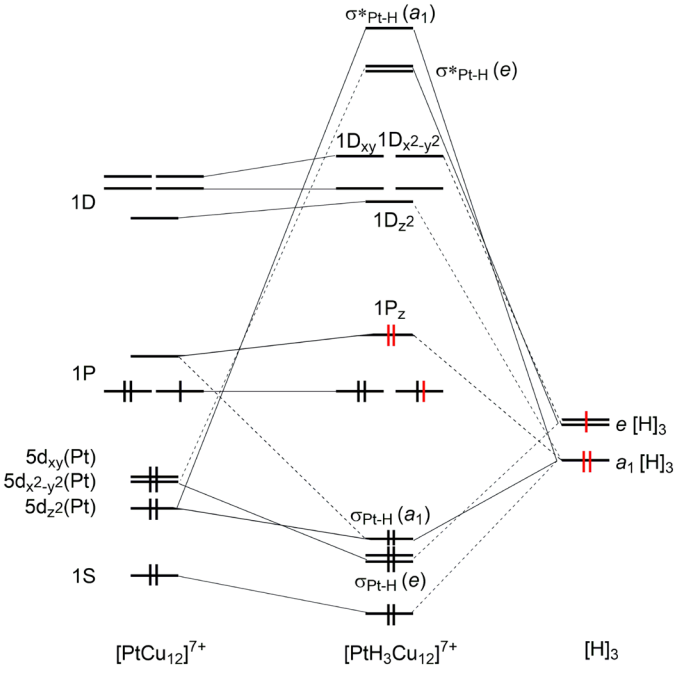

Fig. 5. Simplified interaction MO diagram between the $[PtH_3Cu_{12}]^{7+}$ and $[H]_3$ fragments in the eight-electron superatomic $[PtH_3Cu_{12}]^{7+}$ core in C_3 symmetry.

but nonnegligible participation of 5d(Pt) ($5d_{z2}$, $5d_{xy}$, and $5d_{x2-y2}$) orbitals. These values are slightly larger than those calculated in related species with electron-donating hydrides (*36*, *41*). Thus, the 1s(H) electrons of three interstitial hydrogen atoms contribute to the cluster total electron count of eight in a similar way as the 4s(Cu) electrons. From this point of view, they can be qualified as electron-donating hydrides (*27*, *34*–*38*). In addition, the H-Pt-H angles of 108° allow us also to look at Pt as a sp^3-hybridized metal, as it is in typical 18-electron organometallic complexes. Such extreme limit view describing the PtH_3Cu_{23} as made of a hypothetical 18-electron $[PtH_3]^{5-}$ complex stabilized in a $[Cu_{12}]^{12+}$ cage. This would locate the eight electrons only on the PtH_3 backbone, two of them corresponding to a Pt(sp^3) lone pair (fig. S22). However, calculations on the $[PtH_3Cu_{12}]^{7+}$ kernel indicate a nonnegligible localization of the jellium orbitals containing the eight electrons on the Cu_{12} cage (fig. S23), suggesting that these eight elections behave more like delocalized free electrons in superatoms rather than the valence electrons in common organometallic complexes.

Considering the fact that the electrons of the encapsulated hydrides participate to the superatom electron count, contributing three supplementary free electrons to $PtH_3Cu_{23}(SMe)_{18}(PMe_3)_4$, it is easy to predict an isoelectronic cluster model, $[PtCu_{23}(SMe)_{18}(PMe_3)_4]^{3-}$, by replacing the hydrides with three additional electrons. The optimized structure of the resulting cluster $[PtCu_{23}(SMe)_{18}(PMe_3)_4]^{3-}$ exhibits a slightly distorted cuboctahedral Pt@Cu_{12} kernel with a decreased average Pt-Cu distances, which is more compact than the anticuboctahedral kernel in PtH_3Cu_{23} (fig. S23). Further analysis of the MO diagram of the $[PtCu_{23}(SMe)_{18}(PMe_3)_4]^{3-}$ model indicates a regular eight-electron superatom, with the low-lying (this time) fully occupied 5d (Pt) combinations keeping their nonbonding nature (fig. S24). To the best of our knowledge, a noble metal superatom containing three interstitial electron-donating hydrides has never been reported (*27*, *34*–*38*). The previous computational study reported by Hu *et al.* (*33*) on the well-known $[MAu_{24}(SR)_{18}]^q$ (M = CuH, AgH, AuH, AuH_2, PdH_2, and PtH_2; $q = 0$ and 1) model shows that the third hydrogen cannot be encapsulated within the icosahedral MAu_{12} kernel. The current work on PtH_3Cu_{23} with anticuboctahedral $PtCu_{12}$ kernel however suggests that the key to hydrogen encapsulation may be the structural fluxionality of the cluster kernel structure (*33*). Furthermore, the quasi-tetrahedral architecture of PtH_3Cu_{23} indicates that there is a possible room to include the forth μ_4-H along the C_3 axis, resulting in hypothetical tetrahydrides containing the eight-electron $[MH_4Cu_{23}(SR)_{18}(PR_3)_4]$ (M = Rh for example) structure. This hypothesis pointed the way for the synthesis of copper clusters containing more electron-donating hydrides, strongly encouraging further explorations of the limitation of the number of interstitial electron-donating hydrides encapsulated within an M_{13} architecture, which enriches the structural chemistry of the hydride-containing metal nanoclusters with distinct bonding and electronic properties.

The simulated UV-vis spectrum of PtH_3Cu_{23} was obtained from time-dependent (TD) DFT calculations at the B3LYP/Def2SVP level (see the "Computational details" section in Materials and Methods). It is in good agreement with the experimental spectrum (fig. S25), with an experimentally non-observed HOMO → LUMO transition calculated at 881 nm (α) and two major absorption bands at 481 nm (β) and 360 nm (γ), respectively (fig. S26). The electron-hole analysis based on the natural transition orbitals (NTOs) method was conducted to investigate the nature of these dominant excitation

processes (fig. S26). The lowest transition α, with a very weak oscillator strength, is of metal-to-metal charge transfer (MMCT) from the superatomic 1P type HOMO to the 1D LUMO (fig. S26). The β band is mainly of 5d(Pt)/3d(Cu) →1D (MMCT) nature, whereas the highest energy band γ is of mixed MMCT and ligand-to-metal charge transfer nature, involving transitions from 3d(Cu)/π (ligands)–type orbitals to the 1D/1F-type orbitals (fig. S24).

Stability of the PtH_3Cu_{23} cluster

The stability of the PtH_3Cu_{23} cluster is highly dependent on the conditions. The TD powder x-ray diffraction of PtH_3Cu_{23} crystals in air is shown in fig. S27. The results indicate that the spectral characteristics of the clusters remained unchanged for at least 12 hours, providing evidence of their high stability in an air environment. As shown in figs. S28 and S29, the TD UV-vis and ^{1}H NMR spectra of PtH_3Cu_{23} remain consistent for 6 days when stored in solution form in air. In addition, the UV-vis spectra of the cluster remained unchanged for 6 days when treated with strong reductants (200 eq. triisopropylsilane), acids (200 eq. acetic acid), and bases (200 eq. Et_3N), confirming the cluster's high robustness, as shown in fig. S30. The high stability of the PtH_3Cu_{23} nanocluster is probably attributed to multiple factors, including strong interactions between Pt and Cu atoms, the rigidity of its outermost protective shell, and its closed-shell superatomic nature. However, it should be noted that the cluster exhibits reduced stability when subjected to light irradiation (wavelength, 490 to 500 nm), exposure to oxygen, and heating (at a specific temperature of 60°C). Further endeavors are required to improve the stability of copper superatom NCs in diverse conditions.

DISCUSSION

In summary, we report the synthesis, total structure, and electronic structure analysis of an unprecedented trihydride complex containing an eight-electron Pt/Cu superatomic cluster, PtH_3Cu_{23}(iso-propyl-PhS)$_{18}$(PPh$_3$)$_4$. Its molecular structure features a $[PtH_3Cu_{12}]^{7+}$ superatomic core, protected by an outer sphere of $[Cu_{11}$(iso-propyl-PhS)$_{18}$(PPh$_3$)$_4]^{7-}$. The three hydride atoms are encapsulated within a distorted Pt-centered Cu_{12} anticuboctahedral kernel, each located within a $PtCu_3$ tetrahedron and exhibiting a strong Pt-H interaction. DFT calculations indicate that the three interstitial hydrogens act as donor atoms and provide their 1s(H) electrons to the total superatomic electron count of eight, resulting in a closed-shell eight-electron superatom with a $1S^21P^6$ electron configurations. In other words, the 1s(H) orbitals interact moderately with the superatomic orbitals but more substantially with the 5d(Pt) AOs to form three $\sigma_{Pt\text{-}H}$ bonding orbitals, thus inducing the complete filling of the superatomic 1P shell. In comparison to the previously reported electron-donating hydrides encapsulated in coinage metal superatoms containing icosahedral M_{12} (M = Au and Ag) cluster kernels (*33*–*36*, *41*), the isolation of the PtH_3Cu_{23} with an anticuboctahedral Cu_{12} kernel indicates that the encapsulation of more than two electron-donating hydrides will lead to a substantial structural variation of the cluster kernel. This also reveals the key to the structural evolution from the dihydride containing the icosahedral M_{12} cage to the trihydride containing the anticuboctahedral M_{12} cage, which points the way for constructing high-nuclearity coinage metal clusters that contain more electron-donating hydrides and higher magic electron numbers. This work not only provides a fresh insight into how to encapsulate more electron-donating hydrides within a cluster unit but also enriches the synthetic and structural chemistry of the family of electron-donating hydrides encapsulated metal superatoms.

MATERIALS AND METHODS

Chemicals

4-Isopropylthiophenol ($C_9H_{12}S$, 97%), chloroplatinic acid (H_2PtCl_6, 99%), bis-(triphenylphosphino)-cuprous borohydride [Cu(PPh$_3$)$_2$BH$_4$, 98%], copper (II) sulfate pentahydrate ($CuSO_4$•$5H_2O$, 99%), copper (II) acetate ($C_4H_6CuO_4$, 98%), copper (II) trifluoroacetate ($C_4H_2CuF_6O_5$, 95%), copper(II) dinitrate (CuN_2O_6, 95%), copper (II) acetylacetonate ($C_{10}H_{14}CuO_4$, 97%), copper (II) bromide ($CuBr_2$, 95%), copper (II) gluconate ($C_{12}H_{22}CuO_{14}$, 95%), bis(8-quinolinolato) copper (II) ($C_{18}H_{12}CuN_2O_2$, 97%), copper (II) dibutyldithiocarbamate ($C_{18}H_{36}CuN_2S_4$, 99%), copper (II) citrate ($C_6H_5Cu_2O_7$, 99.5%), copper (I) thiocyanate (CuSCN, 98%), copper (II) pyrithione ($C_{10}H_{10}CuN_2O_2S_2$, 95%), copper (II) trifluoromethanesulfonate ($C_2CuF_6O_6S_2$, 98%), copper (I) chloride (CuCl, 99%), and copper (II) sulfate, anhydrous ($CuSO_4$, 98%) were purchased from Bidepharm (Shanghai, China). Copper (II) tartrate hydrate ($C_4H_6CuO_7$, 98%) was purchased from Acmec Biochemical (Shanghai, China). Copper (II) phosphate ($Cu_3P_2O_8$, 99%) was purchased from Leyan (Shanghai, China). Dichloromethane-d_2 (CD_2Cl_2, D, 99.8%), chloroform-d ($CDCl_3$, D, 99.8%), toluene (C_7H_8, Analytical Reagent), dichloromethane (CH_2Cl_2, Analytical Reagent), ethanol (C_2H_5OH, Analytical Reagent), methanol (CH_3OH, Analytical Reagent), and ether ($C_4H_{10}O$, Analytical Reagent) were purchased from Sinopharm Chemical Reagent Co. Ltd. (Shanghai, China). The water used in all experiments was ultrapure (18.25 Mohm). All reagents were used without further purification. Copper (II) diclofenac, Cu(MeCN)$_4$BF$_4$, Cu(L-valine)$_2$, Cu(L-isoleucine)$_2$, Cu(L-threonine)$_2$, Cu(L-proline)$_2$, Cu(L-phenylalanine)$_2$, and Cu(L-alanine)$_2$ were prepared according to the methods described in the literature (*62*–*64*).

Characterization of PtH_3Cu_{23} nanoclusters

Ultraviolet-visible spectroscopy

The UV-vis absorption spectroscopy of the PtH_3Cu_{23} cluster was collected by a UV-650 spectrophotometer, using a 1-mm optical path length quartz cuvette at a scanning speed of 400 nm/min.

High-resolution electrospray ionization mass spectrometry

The crystals of PtH_3Cu_{23} were dissolved in CH_2Cl_2 [high-performance liquid chromatography (HPLC) grade] and configured into a solution with an appropriate concentration. A trace amount of formic acid (HPLC grade) was added to promote efficient ionization. The solution was injected directly with an injection pump at a flow rate of 1.2 ml/hour. The positive ion ESI-MS was recorded by an Agilent 6546 Liquid Chromatography/Quadrupole Time-of-Flight LMS spectrometer.

Powder x-ray diffraction

Powder x-ray diffraction data of the samples were collected on a Bruker D8 advanced diffractometer with Cu-Kα radiation (λ = 1.5418 Å) at a scan rate of 0.038° s^{-1}.

X-ray single-crystal diffraction

The molecular structure of PtH_3Cu_{23} was determined on the x-ray single crystal diffractometer of the Agilent Technologies SuperNova system. The temperature during measurement was 100 K, and the incident light source used was Cu-Kα ray (λ = 1.54184 Å). The absorption correction was carried out using the CrysAlis^{pro} program.

For structure analysis and refinement, the software Olex2 (*65*), ShelXT (*66*), and ShelXL (*67*) were used. All nonhydrogen atoms were identified on the basis of full-matrix least-squares refinement on F^2. The SHELXTL restraint instructions DFIX, DANG, ISOR, SADI, and RIGU were applied to these disordered groups to keep their geometries and atomic displacement parameters reasonably. All host framework nonhydrogen atoms were refined anisotropically (*68*). All hydrogen atoms on organic ligands were produced symmetrically (C—H = 0.96 Å). The thermal ellipsoids of the Oak Ridge thermal ellipsoid plot diagram were done at 50% probability. Detailed crystal data and structure refinements for the compound can be found in table S11.

Nuclear magnetic resonance spectroscopy

NMR spectra were recorded on a Bruker AV-600 MHz NMR spectrometer. The chemical shift is reported in parts per million with the solvent residue peak as an internal standard. All NMR data were processed on MestReNova software.

X-ray photoelectron spectroscopy

The XPS data of PtH_3Cu_{23} were performed on the ESCALABXI+ System (Thermo Fisher Scientific, UK). The C 1s peak of adventitious carbon (284.8 eV) was used for position correction in all cases.

Computational details

DFT calculations were performed using the ADF2020 program (*69*), incorporating scalar relativistic corrections via the zeroth-order regular approximation Hamiltonian (*70*). Geometry optimizations were carried out using a triple-ξ Slater basis set, plus two polarization functions (STO-TZ2P) (*71*), under the generalized gradient approximation level of theory together with the Becke-Perdew exchange and correlation functional (BP86) (*72*). Grimme's DFT-D3-BJ empirical corrections (*73*) were used to take into account the dispersion effect. The optimized structures were confirmed as the true minima on their potential surface by analytical vibrational frequency calculations. To reduce computational efforts, the Gaussian16 package (*74*) was used to calculate the UV-vis optical transitions by TD-DFT (*75*) calculations, using the Def2SVP (*76*) basis set (which includes effective core potentials accounting for scalar relativistic effects of Pt) and B3LYP (*77*) functional. The UV-vis spectrum were simulated from the computed transition energies and their oscillator strengths, with each transition being associated with a Gaussian function of half-height width equal to 2400 cm^{-1}, a value that best reproduces the experimental spectrum. NTOs were generated by using Multiwfn (*78*) software with an isosurface value of ±0.02 (e/bohr3) 1/2.

Synthesis of PtH_3Cu_{23}(iso-propyl-PhS)$_{18}$(PPh_3)$_4$

Thirty milligrams of Cu(L-valine)$_2$ (0.1 mmol) was suspended in 1 ml of methanol and 2 ml of dichloromethane. To this mixture, 1 mg of H_2PtCl_6 (0.002 mmol) was added. The resulting mixture was stirred for 5 min, followed by the addition of 8.4 μl of 4-isopropylphenthiol (0.56 mmol) once. The mixture was then stirred at room temperature for an additional 5 min before the dropwise addition of a dichloromethane solution of $Cu(PPh_3)_2BH_4$ (40 mg, 0.06 mmol, 1 ml). During the stirring process, the solution gradually changed from gray-green to reddish-brown, and the stirring was continued for 3 hours. Subsequently, the mixture was centrifuged at a speed of 10,000 rpm/min for 2 min. The supernatant was carefully collected and transferred to a crystallization tube, ensuring that no precipitation was present in the supernatant. The red solution was subjected to diffusion of ether in the dark. After a period of 2 weeks, clean red crystals were obtained and stored in the refrigerator for future use (yield: 71.7%, based on Cu).

Synthesis of PtD_3Cu_{23}(iso-propyl-PhS)$_{18}$(PPh_3)$_4$

The PtD_3Cu_{23} cluster was synthesized using a comparable procedure to PtH_3Cu_{23}, with the only variation being the substitution of $Cu(PPh_3)_2BD_4$ for $Cu(PPh_3)_2BH_4$ as the reducing agent in the synthesis.

Stability tests

Air stability studies

The stock solution of PtH_3Cu_{23} was placed in a refrigerator at 2°C and then characterized within 6 days using UV-vis spectroscopy (toluene solution) and ^{1}H NMR spectroscopy (CD_2Cl_2 solution).

pH stability studies

The toluene stock solution of PtH_3Cu_{23} was treated with 200 eq. of CH_3COOH or 200 eq. of Et_3N. The mixed solution was stored in a refrigerator at 2°C and then characterized within 6 days using UV-vis spectroscopy (toluene solution).

Reductant stability studies

The toluene stock solution of PtH_3Cu_{23} was treated with 200 eq. ^{i}Pr$_3$SiH. The mixed solution was stored in a refrigerator at 2°C and measured and then characterized within 6 days using UV-vis spectroscopy (toluene solution).

Photostability studies

The stock solution of PtH_3Cu_{23} was placed under light irradiation with a wavelength range of 490 to 500 nm and maintained in an ice bath. The sample was continuously characterized by UV-vis spectroscopy (toluene solution) for a period of 12 hours.

Oxygen stability studies

First, the Schlenk tube was evacuated, and then the PtH_3Cu_{23} stock solution was injected. Oxygen gas was introduced into the tube at room temperature. The sample was continuously characterized by UV-vis spectroscopy (toluene solution) for a period of 12 hours.

Thermal stability studies

The PtH_3Cu_{23} stock solution was heated in an oil bath at 60°C. The sample was continuously characterized by UV-vis spectroscopy (toluene solution) for a period of 12 hours.

Supplementary Materials

This PDF file includes:

Figs. S1 to S30

Tables S1 to S11

REFERENCES AND NOTES

1. R. Jin, C. Zeng, M. Zhou, Y. Chen, Atomically precise colloidal metal nanoclusters and nanoparticles: Fundamentals and opportunities. *Chem. Rev.* **116**, 10346–10413 (2016).
2. I. Chakraborty, T. Pradeep, Atomically precise clusters of noble metals: Emerging link between atoms and nanoparticles. *Chem. Rev.* **117**, 8208–8271 (2017).
3. M. R. Narouz, K. M. Osten, P. J. Unsworth, R. W. Y. Man, K. Salorinne, S. Takano, R. Tomihara, S. Kaappa, S. Malola, C. T. Dinh, J. D. Padmos, K. Ayoo, P. J. Garrett, M. Nambo, J. H. Horton, E. H. Sargent, H. Häkkinen, T. Tsukuda, C. M. Crudden, N-heterocyclic carbene-functionalized magic-number gold nanoclusters. *Nat. Chem.* **11**, 419–425 (2019).
4. K. Yonesato, S. Yamazoe, D. Yokogawa, K. Yamaguchi, K. Suzuki, A molecular hybrid of an atomically precise silver nanocluster and polyoxometalates for H_2 cleavage into protons and electrons. *Angew. Chem. Int. Ed.* **60**, 16994–16998 (2021).

5. M. Walter, J. Akola, O. L. Acevedo, P. D. Jadzinsky, G. Calero, C. J. Ackerson, R. L. Whetten, H. Gronbeck, H. Häkkinen, A unified view of ligand-protected gold clusters as superatom complexes. *Proc. Natl. Acad. Sci. U.S.A.* **105**, 9157–9162 (2008).
6. W. D. Knight, K. Clemenger, W. A. de Heer, W. A. Saunders, M. Y. Chou, M. L. Cohen, Electronic shell structure and abundances of sodium clusters. *Phys. Rev. Lett.* **52**, 2141–2143 (1984).
7. D. M. P. Mingos, T. Slee, L. Zhenyang, Bonding models for ligated and bare clusters. *Chem. Rev.* **90**, 383–402 (1990).
8. K. Chakrahari, J. Liao, R. P. B. Silalahi, T. Chiu, J. Liao, X. Wang, S. Kahlal, J. Saillard, C. W. Liu, Isolation and structural elucidation of 15-Nuclear copper dihydride clusters: An intermediate in the formation of a two-electron copper superatom. *Small* **17**, e2002544 (2021).
9. T. Jia, Z. J. Guan, C. Zhang, X. Z. Zhu, Y. X. Chen, Q. Zhang, Y. Yang, D. Sun, Eight-electron superatomic Cu_{31} nanocluster with chiral kernel and NIR-II emission. *J. Am. Chem. Soc.* **145**, 10355–10363 (2023).
10. S. Sharma, K. K. Chakrahari, J. Saillard, C. W. Liu, Structurally precise dichalcogenolate-protected copper and silver superatomic nanoclusters and their alloys. *Acc. Chem. Res.* **51**, 2475–2483 (2018).
11. J. Weßing, C. Ganesamoorthy, S. Kahlal, R. Marchal, C. Gemel, O. Cador, A. C. H. Da Silva, J. L. F. Da Silva, J. Saillard, R. A. Fischer, The mackay-type cluster $[Cu_{43}Al_{12}](Cp^*)_{12}$: Open-shell 67-electron superatom with emerging metal-like electronic structure. *Angew. Chem. Int. Ed.* **57**, 14630–14634 (2018).
12. B. Zouchoune, J. Saillard, Atom-Precise ligated copper and copper-rich nanoclusters with mixed-valent Cu(I)/Cu(0) character: Structure–electron count relationships. *Molecules.* **29**, (2024).
13. R. S. Dhayal, W. E. van Zyl, C. W. Liu, Polyhydrido copper clusters: Synthetic advances, structural diversity, and nanocluster-to-nanoparticle conversion. *Acc. Chem. Res.* **49**, 86–95 (2016).
14. A. J. Jordan, G. Lalic, J. P. Sadighi, Coinage metal hydrides: Synthesis, characterization, and reactivity. *Chem. Rev.* **116**, 8318–8372 (2016).
15. C. M. Zall, J. C. Linehan, A. M. Appel, Triphosphine-ligated copper hydrides for CO_2 hydrogenation: Structure, reactivity, and thermodynamic studies. *J. Am. Chem. Soc.* **138**, 9968–9977 (2016).
16. C. Sun, N. Mammen, S. Kaappa, P. Yuan, G. Deng, C. Zhao, J. Yan, S. Malola, K. Honkala, H. Häkkinen, B. K. Teo, N. F. Zheng, Atomically precise, thiolated copper–hydride nanoclusters as single-site hydrogenation catalysts for ketones in mild conditions. *ACS Nano* **13**, 5975–5986 (2019).
17. W. E. van Zyl, C. W. Liu, Interstitial hydrides in nanoclusters can reduce M(I) (M=Cu, Ag, Au) to M(0) and form stable superatoms. *Chem. Eur. J.* **28**, e202104241 (2022).
18. P. K. Liao, C. S. Fang, A. J. Edwards, S. Kahlal, J. Y. Saillard, C. W. Liu, Hydrido copper clusters supported by dithiocarbamates: Oxidative hydride removal and neutron diffraction analysis of $[Cu_7(H)\{S_2C(\text{aza-15-crown-5})\}_6]$. *Inorg. Chem.* **51**, 6577–6591 (2012).
19. T. Chiu, J. Liao, R. P. B. Silalahi, M. N. Pillay, C. W. Liu, Hydride-doped coinage metal superatoms and their catalytic applications. *Nanoscale Horiz.* **9**, 675–692 (2024).
20. X. Liu, E. Wang, M. Zhou, Y. Wan, Y. Zhang, H. Liu, Y. Zhao, J. Li, Y. Gao, Y. Zhu, Asymmetrically doping a platinum atom into a Au_{38} nanocluster for changing the electron configuration and reactivity in electrocatalysis. *Angew. Chem. Int. Ed.* **61**, e202207685 (2022).
21. A. Ghosh, O. F. Mohammed, O. M. Bakr, Atomic-level doping of metal clusters. *Acc. Chem. Res.* **51**, 3094–3103 (2018).
22. M. Kim, Q. Tang, A. V. Narendra Kumar, K. Kwak, W. Choi, D. Jiang, D. Lee, Dopant-dependent electronic structures observed for $M_2Au_{36}(SC_6H_{13})_{24}$ clusters (M = Pt, Pd). *J. Phys. Chem. Lett.* **9**, 982–989 (2018).
23. S. Hossain, T. Ono, M. Yoshioka, G. Hu, M. Hosoi, Z. Chen, L. V. Nair, Y. Niihori, W. Kurashige, D. Jiang, Y. Negishi, Thiolate-protected trimetallic $Au_{\sim 20}Ag_{\sim 4}Pd$ and $Au_{\sim 20}Ag_{\sim 4}Pt$ Alloy clusters with controlled chemical composition and metal positions. *J. Phys. Chem. Lett.* **9**, 2590–2594 (2018).
24. K. Kwak, W. Choi, Q. Tang, M. Kim, Y. Lee, D. E. Jiang, D. Lee, A molecule-like $PtAu_{24}S(C_6H_{13})_{18}$ nanocluster as an electrocatalyst for hydrogen production. *Nat. Commun.* **8**, 14723 (2017).
25. S. K. Barik, T. Chiu, Y. Liu, M. Chiang, F. Gam, I. Chantrenne, S. Kahlal, J. Saillard, C. W. Liu, Mono- and hexa-palladium doped silver nanoclusters stabilized by dithiolates. *Nanoscale* **11**, 14581–14586 (2019).
26. R. P. Brocha Silalahi, H. Liang, Y. Jo, J. Liao, T. Chiu, Y. Wu, X. Wang, S. Kahlal, Q. Wang, W. Choi, D. Lee, J. Saillard, C. W. Liu, Hydride-containing Pt-doped Cu-rich nanoclusters: Synthesis, structure, and electrocatalytic hydrogen evolution. *Chem. Eur. J.* **30**, e202303755 (2024).
27. R. P. Brocha Silalahi, Y. Jo, J. Liao, T. Chiu, E. Park, W. Choi, H. Liang, S. Kahlal, J. Saillard, D. Lee, C. W. Liu, Hydride-containing 2-electron Pd/Cu superatoms as catalysts for efficient electrochemical hydrogen evolution. *Angew. Chem. Int. Ed.* **62**, e202301272 (2023).
28. K. K. Chakrahari, R. P. B. Silalahi, T. Chiu, X. Wang, N. Azrou, S. Kahlal, Y. Liu, M. Chiang, J. Saillard, C. W. Liu, Synthesis of bimetallic copper-rich nanoclusters encapsulating a linear palladium dihydride unit. *Angew. Chem. Int. Ed.* **58**, 4943–4947 (2019).
29. A. Cirri, H. M. Hernández, C. J. Johnson, Hydride, chloride, and bromide show similar electronic effects in the $Au_9(PPh_3)_8^{3+}$ nanocluster. *Chem. Commun.* **56**, 1283–1285 (2020).
30. Q. Tang, Y. Lee, D. Li, W. Choi, C. W. Liu, D. Lee, D. Jiang, Lattice-hydride mechanism in electrocatalytic CO_2 reduction by structurally precise copper-hydride nanoclusters. *J. Am. Chem. Soc.* **139**, 9728–9736 (2017).
31. X. Yuan, C. Sun, X. Li, S. Malola, B. K. Teo, H. Hakkinen, L. S. Zheng, N. F. Zheng, Combinatorial identification of hydrides in a ligated Ag_{40} nanocluster with noncompact metal core. *J. Am. Chem. Soc.* **141**, 11905–11911 (2019).
32. H. Shen, L. Wang, O. López-Estrada, C. Hu, Q. Wu, D. Cao, S. Malola, B. K. Teo, H. Häkkinen, N. F. Zheng, Copper-hydride nanoclusters with enhanced stability by N-heterocyclic carbenes. *Nano Res.* **14**, 3303–3308 (2021).
33. G. Hu, Q. Tang, D. Lee, Z. Wu, D. Jiang, Metallic hydrogen in atomically precise gold nanoclusters. *Chem. Mater.* **29**, 4840–4847 (2017).
34. H. Yi, S. M. Han, S. Song, M. Kim, E. Sim, D. Lee, Superatom-in-superatom $[RhH@Ag_{24}(SPhMe_2)_{18}]^{2-}$ nanocluster. *Angew. Chem. Int. Ed.* **60**, 22293–22300 (2021).
35. H. Yi, S. Song, S. M. Han, J. Lee, W. Kim, E. Sim, D. Lee, Superatom-in-superatom nanoclusters: Synthesis, structure, and photoluminescence. *Angew. Chem. Int. Ed.* **62**, e202302591 (2023).
36. T. Chiu, J. Liao, F. Gam, Y. Wu, X. Wang, S. Kahlal, J. Saillard, C. W. Liu, Hydride-containing eight-electron Pt/Ag superatoms: Structure, bonding, and multi-NMR studies. *J. Am. Chem. Soc.* **144**, 10599–10607 (2022).
37. S. Takano, H. Hirai, S. Muramatsu, T. Tsukuda, Hydride-doped gold superatom $(Au_9H)^{2+}$: Synthesis, structure, and transformation. *J. Am. Chem. Soc.* **140**, 8380–8383 (2018).
38. S. Takano, H. Hirai, S. Muramatsu, T. Tsukuda, Hydride-mediated controlled growth of a bimetallic $(Pd@Au_8)^{2+}$ superatom to a hydride-doped $(HPd@Au_{10})^{3+}$ superatom. *J. Am. Chem. Soc.* **140**, 12314–12317 (2018).
39. S. Maity, S. Takano, S. Masuda, T. Tsukuda, Bonding and electronic interactions of hydrogen with gold superatoms. *J. Phys. Chem. C* **128**, 19–30 (2024).
40. T. Chiu, M. N. Pillay, Y. Wu, Y. Niihori, Y. Negishi, J. Chen, Y. J. Chen, S. Kahlal, J. Saillard, C. W. Liu, Controlled aggregation of Pt/PtH/Rh/RhH doped silver superatomic nanoclusters into 16-electron supermolecules. *Chem. Sci.* **15**, 14660–14667 (2024).
41. T. Chiu, J. Liao, Y. Wu, J. Chen, Y. Chen, X. Wang, S. Kahlal, J. Saillard, C. W. Liu, Hydride doping effects on the structure and properties of eight-electron Rh/Ag superatoms: The $[RhH_x@Ag_{21-x}\{S_2P(O^nPr)_2\}_{12}]$ (x = 0–2) series. *J. Am. Chem. Soc.* **145**, 16739–16747 (2023).
42. R. W. Huang, J. Yin, C. Dong, P. Maity, M. N. Hedhili, S. Nematulloev, B. Alamer, A. Ghosh, O. F. Mohammed, O. M. Bakr, $[Cu_{23}(PhSe)_{16}(Ph_3P)_8(H)_6]\cdot BF_4$: Atomic-level insights into cuboidal polyhydrido copper nanoclusters and their quasi-simple cubic self-assembly. *ACS Materials Lett.* **3**, 90–99 (2021).
43. T. G. M. M. Kappen, P. P. J. Schlebos, J. J. Bour, W. P. Bosman, G. Beurskens, J. M. M. Smits, P. T. Beurskens, J. J. Steggerda, Cluster growth: Some representative reactions. Crystal structures of $[Pt(H)(AgNO_3)(AuPPh_3)_8](NO_3)$ and $[Pt(H)(AgNO_3)_2(AuPPh_3)_8](NO_3)$. *Inorg. Chem.* **34**, 2121–2132 (1995).
44. S. Lee, M. S. Bootharaju, G. Deng, S. Malola, H. Häkkinen, N. F. Zheng, T. Hyeon, $[Pt_2Cu_{34}(PET)_{22}Cl_4]^{2-}$: An atomically precise, 10-electron PtCu bimetal nanocluster with a direct Pt–Pt bond. *J. Am. Chem. Soc.* **143**, 12100–12107 (2021).
45. J. H. Liao, R. P. Brocha Silalahi, T. Chiu, C. W. Liu, Locating interstitial hydrides in $MH_2@Cu_{14}$ (M = Cu, Ag) clusters by single-crystal x-ray diffraction. *ACS Omega* **8**, 31541–31547 (2023).
46. Y. R. Ni, M. N. Pillay, T. H. Chiu, Y. Y. Wu, S. Kahlal, J. Y. Saillard, C. W. Liu, Controlled shell and kernel modifications of atomically precise Pd/Ag superatomic nanoclusters. *Chem. Eur. J.* **29**, e202300730 (2023).
47. K. K. Chakrahari, J. Liao, S. Kahlal, Y. Liu, M. Chiang, J. Saillard, C. W. Liu, $[Cu_{13}\{S_2CN^nBu_2\}_6(\text{acetylide})_4]+$: A two-electron superatom. *Angew. Chem. Int. Ed.* **55**, 14704–14708 (2016).
48. H. Zabrodsky, S. Peleg, D. Avnir, Continuous symmetry measures. *J. Am. Chem. Soc.* **114**, 7843–7851 (1992).
49. S. Zhang, S. Havenridge, C. Zhang, Z. Wang, L. Feng, Z. Y. Gao, C. M. Aikens, C. H. Tung, D. Sun, Sulfide boosting near-unity photoluminescence quantum yield of silver nanocluster. *J. Am. Chem. Soc.* **144**, 18305–18314 (2022).
50. Y. Zeng, S. Havenridge, M. Gharib, A. Baksi, K. L. D. M. Weerawardene, A. Ziefuß, C. Strelow, C. Rehbock, A. Mews, S. Barcikowski, M. M. Kappes, W. J. Parak, C. M. Aikens, I. Chakraborty, Impact of ligands on structural and optical properties of Ag_{29} nanoclusters. *J. Am. Chem. Soc.* **143**, 9405–9414 (2021).
51. J. Wei, S. Kahlal, J. Halet, A. Muñoz-Castro, J. Saillard, Ligand-induced cuboctahedral versus icosahedral core isomerism within eight-electron heterocyclic-carbene-protected gold nanoclusters. *Inorg. Chem.* **61**, 8623–8628 (2022).
52. J. Wei, D. MacLeod Carey, J. Halet, S. Kahlal, J. Saillard, A. Muñoz-Castro, From 8- to 18-cluster electrons superatoms: Evaluation via DFT calculations of the ligand-protected

W@Au_{12}(dppm)$_6$ cluster displaying distinctive electronic and optical properties. *Inorg. Chem.* **62**, 3047–3055 (2023).
53. Z. Gao, K. Wei, T. Wu, J. Dong, D. Jiang, S. Sun, L. Wang, A heteroleptic gold hydride nanocluster for efficient and selective electrocatalytic reduction of CO_2 to CO. *J. Am. Chem. Soc.* **144**, 5258–5262 (2022).
54. M. Zhou, T. Higaki, G. Hu, M. Y. Sfeir, Y. Chen, D. Jiang, R. Jin, Three-orders-of-magnitude variation of carrier lifetimes with crystal phase of gold nanoclusters. *Science* **364**, 279–282 (2019).
55. R. S. Dhayal, J. H. Liao, X. Wang, Y. C. Liu, M. H. Chiang, S. Kahlal, J. Y. Saillard, C. W. Liu, Diselenophosphate-induced conversion of an achiral $[Cu_{20}H_{11}\{S_2P(O^iPr)_2\}_9]$ into a Chiral $[Cu_{20}H_{11}\{Se_2P(O^iPr)_2\}_9]$ polyhydrido nanocluster. *Angew. Chem. Int. Ed.* **54**, 13604–13608 (2015).
56. R. S. Dhayal, J. H. Liao, S. Kahlal, X. Wang, Y. C. Liu, M. H. Chiang, W. E. van Zyl, J. Y. Saillard, C. W. Liu, $[Cu_{32}(H)_{20}\{S_2P(O^iPr)_2\}_{12}]$: The largest number of hydrides recorded in a molecular nanocluster by neutron diffraction. *Chem. Eur. J.* **21**, 8369–8374 (2015).
57. R. P. B. Silalahi, J. H. Liao, Y. F. Tseng, T. H. Chiu, S. Kahlal, J. Y. Saillard, C. W. Liu, Unusual core engineering on a copper hydride nanoball. *Dalton Trans.* **52**, 2106–2114 (2023).
58. R. P. Brocha Silalahi, G. Huang, J. Liao, T. Chiu, K. K. Chakrahari, X. Wang, J. Cartron, S. Kahlal, J. Saillard, C. W. Liu, Copper clusters containing hydrides in trigonal pyramidal geometry. *Inorg. Chem.* **59**, 2536–2547 (2020).
59. C. W. Liu, Y. Lin, C. Fang, C. Latouche, S. Kahlal, J. Saillard, $[Ag_7(H)\{E_2P(OR)_2\}_6]$ (E = Se, S): Precursors for the fabrication of silver nanoparticles. *Inorg. Chem.* **52**, 2070–2077 (2013).
60. R. S. Dhayal, J. Liao, Y. Lin, P. Liao, S. Kahlal, J. Saillard, C. W. Liu, A nanospheric polyhydrido copper cluster of elongated triangular orthobicupola array: Liberation of H_2 from solar energy. *J. Am. Chem. Soc.* **135**, 4704–4707 (2013).
61. J. Wei, P. L. Rodríguez-Kessler, J. Halet, S. Kahlal, J. Saillard, A. Muñoz-Castro, On heteronuclear isoelectronic alternatives to $[Au_{13}(dppe)_5Cl_2]^{3+}$: Electronic and optical properties of the 18-electron Os@$[Au_{12}(dppe)_5Cl_2]$ cluster from relativistic density functional theory computations. *Inorg. Chem.* **60**, 8173–8180 (2021).
62. B. Yan, X. You, X. Tang, J. Sun, Q. Xu, L. Wang, Z. J. Guan, F. Li, H. Shen, Carboxylate-protected "isostructural" Cu_{20} nanoclusters as a model system: Carboxylate effect on controlling catalysis. *Chem. Mater.* **36**, 1004–1012 (2024).
63. A. Ghosh, R. W. Huang, B. Alamer, E. Abou-Hamad, M. N. Hedhili, O. F. Mohammed, O. M. Bakr, $[Cu_{61}(S^tBu)_{26}S_6Cl_6H_{14}]^+$: A core–shell superatom nanocluster with a quasi-J_{36} Cu_{19} core and an "18-crown-6" metal-sulfide-like stabilizing belt. *ACS Materials Lett.* **1**, 297–302 (2019).
64. J. Sun, X. Tang, Z. Liu, Z. Xie, B. Yan, R. Yin, C. Chaolumen, J. Zhang, W. Fang, J. Wei, H. Shen, Labile ligands protected Cu_{50} nanoclusters with tailorable optical limiting effect. *ACS Materials Lett.* **6**, 281–289 (2024).
65. O. V. Dolomanov, L. J. Bourhis, R. J. Gildea, J. A. K. Howard, H. Puschmann, OLEX2: A complete structure solution, refinement and analysis program. *J. Appl. Cryst.* **42**, 339–341 (2009).
66. G. M. Sheldrick, SHELXT-integrated space-group and crystal-structure determination. *Acta Cryst. A* **71**, 3–8 (2015).
67. G. M. Sheldrick, A short history of SHELX. *Acta Cryst. A* **64**, 112–122 (2008).
68. Y. Wei, M. Zhang, P. Liao, R. Lin, T. Li, G. Shao, J. Zhang, X. Chen, Coordination templated [2+2+2] cyclotrimerization in a porous coordination framework. *Nat. Commun.* **6**, 8348 (2015).
69. G. te Velde, F. M. Bickelhaupt, E. J. Baerends, C. Fonseca Guerra, S. J. A. van Gisbergen, J. G. Snijders, T. Ziegler, Chemistry with ADF. *J. Comput. Chem.* **22**, 931–967 (2001).
70. E. van Lenthe, E. J. Baerends, J. G. Snijders, Relativistic total energy using regular approximations. *J. Chem. Phys.* **101**, 9783–9792 (1994).
71. E. Van Lenthe, E. J. Baerends, Optimized Slater-type basis sets for the elements 1–118. *J. Comput. Chem.* **24**, 1142–1156 (2003).
72. A. D. Becke, Density-functional exchange-energy approximation with correct asymptotic behavior. *Phys. Rev. A* **38**, 3098–3100 (1988).
73. S. Grimme, Semiempirical GGA-type density functional constructed with a long-range dispersion correction. *J. Comput. Chem.* **27**, 1787–1799 (2006).
74. M. J. Frisch, G. W. Trucks, H. B. Schlegel, G. E. Scuseria, M. A. Robb, J. R. Cheeseman, G. Scalmani, V. Barone, G. A. Petersson, H. Nakatsuji, X. Li, M. Caricato, A. V. Marenich, J. Bloino, B. G. Janesko, R. Gomperts, B. Mennucci, H. P. Hratchian, J. V. Ortiz, A. F. Izmaylov, J. L. Sonnenberg, Williams, F. Ding, F. Lipparini, F. Egidi, J. Goings, B. Peng, A. Petrone, T. Henderson, D. Ranasinghe, V. G. Zakrzewski, J. Gao, N. Rega, G. Zheng, W. Liang, M. Hada, M. Ehara, K. Toyota, R. Fukuda, J. Hasegawa, M. Ishida, T. Nakajima, Y. Honda, O. Kitao, H. Nakai, T. Vreven, K. Throssell, J. A. Montgomery Jr., J. E. Peralta, F. Ogliaro, M. J. Bearpark, J. J. Heyd, E. N. Brothers, K. N. Kudin, V. N. Staroverov, T. A. Keith, R. Kobayashi, J. Normand, K. Raghavachari, A. P. Rendell, J. C. Burant, S. S. Iyengar, J. Tomasi, M. Cossi, J. M. Millam, M. Klene, C. Adamo, R. Cammi, J. W. Ochterski, R. L. Martin, K. Morokuma, O. Farkas, J. B. Foresman, D. J. Fox. Gaussian16, Gaussian, Inc.: Wallingford, CT, 2016.
75. E. Runge, E. K. U. Gross, Density-functional theory for time-dependent systems. *Phys. Rev. Lett.* **52**, 997–1000 (1984).
76. F. Weigend, R. Ahlrichs, Balanced basis sets of split valence, triple zeta valence and quadruple zeta valence quality for H to Rn: Design and assessment of accuracy. *Phys. Chem. Chem. Phys.* **7**, 3297–3305 (2005).
77. A. D. Becke, Density-functional thermochemistry. III. The role of exact exchange. *J. Chem. Phys.* **98**, 5648–5652 (1993).
78. T. Lu, F. Chen, Multiwfn: A multifunctional wavefunction analyzer. *J. Comput. Chem.* **33**, 580–592 (2012).

Acknowledgments: We thank H. Li in the NMR facility of National Center for Protein Sciences at Peking University for assistance with the NMR measurement. **Funding:** H.S. thanks the financial support from the National Key R&D Program of China (2023YFB3507100), National Natural Science Foundation of China (22301149), Program for Young Talents of Science and Technology in Universities of Inner Mongolia Autonomous Region (NJYT23035), and Start-up funding of Inner Mongolia University (10000-23112101/043). N.Z. acknowledges financial support from the National Natural Science Foundation of China (grant no. 92261207), NSFC Center for Single-Atom Catalysis under grant no. 22388102, and the New Cornerstone Science Foundation. **Author contributions:** H.S., J.W., and N.Z. conceived and designed the experiments; A.H., X.T., and L.W. conducted synthesis and characterization; A.H., J.W., and H.S. performed research and analyzed data; D.Z., G.J., L.F., Z.Z., J.W., N.Z., and H.S. contributed to scientific discussion; A.H., J.W., and H.S. wrote the paper. All authors discussed the results and commented on the manuscript. **Competing interests:** The authors declare that they have no competing interests. **Data and materials availability:** All data needed to evaluate the conclusions in the paper are present in the paper and/or the Supplementary Materials. The cif. data of PtH_3Cu_{23} can be obtained free of charge from the Cambridge Crystallographic Data Centre (CCDC): CCDC 2262980 for PtH_3Cu_{23}.

Submitted 15 August 2024
Accepted 4 December 2024
Published 8 January 2025
10.1126/sciadv.ads4488